Evolution of anodic product from Mo metal in absolute ethanol and humidity sensing under an ambient condition

Chengsheng Ni[1,2,3*], Darragh Carolan[2], Jianing Hui[3], Conor Rocks[2], Dilli Babu Padmanaban[2], Zeguo Fang[3], Jiupai Ni[1], Deti Xie[1], Paul Maguire[2], John T.S. Irvine[3] and Davide Mariotti[2]

1 College of Resources and Environment, Southwest University, Beibei, Chongqing, 400716, China

2 School of Engineering, Ulster University, Jordanstown Campus, Shore Road, Newtownabbey, Northern Ireland, UK, BT37 0QB

3 School of Chemistry, University of St Andrews, Fife, KY16 9ST, Scotland, UK

*Email: C.N.: nichengsheg@swu.edu.cn; nichengsheg@163.com

This manuscript contains supporting information including the testing setup, FTIR, SEM, EDS, TGA and et al..

Keywords: microplasma; molybdenum oxide; crystal growth; molybdenum blue; NMR; humidity sensing.

Abstract

Room-temperature non-aqueous synthetic routes turn out to be particularly competitive among all the available liquid-phase synthetic methods for nanometer-sized metal oxides for multiple applications. Microplasma-assisted anodization is employed to prepare soluble and crystalline Mo species in a water-deficient and extraneous ionic-salt-free ethanol electrolyte. The anodization of Mo in absolute ethanol is found to produce Mo oxyethoxide in the liquid ethanol phase along with a small montage of mixed

hexagonal and orthorhombic MoO_3 crystals. The evolution of Mo species in solid and liquid phase is characterized to study the crystallization of MoO_3 crystal and the formation of blue spherical Mo polyoxometalates (POMs) after extended aging. The addition of water in the suspension delayed the formation of molybdenum blue while hydrogen peroxide induced the precipitation of dendritic framework of hexagonal MoO_3. A thin MoO_3 film was produced from the solution and can be used for humidity sensing by the facile conductivity measurement.

■ Introduction

The rapid growth of inorganic nanoparticles prepared by nonaqueous and/or nonhydrolytic processes clearly indicates that synthesis in organic solvents under exclusion of water is a versatile alternative to aqueous methods[1]. However, the liquid phase routes employed to date even with organic solvent including co-precipitation, sol-gel process, solvothermal etc. require the final calcination at moderate temperature to remove the organic material or increase the crystallinity of the inorganic material[2] and the rational synthesis of crystalline materials at room temperature and ambient pressure is still a prominent challenge[2,3]. Recently, hybrid microplasma-liquid electrochemical systems at ambient conditions have been demonstrated as an efficient and green method for the synthesis of nanoparticles, such as metals [4,5], metal oxides[6-8], polymers[9,10] etc. MoO_3 nanocrystals in suspension for the processing of thin films or highly efficient catalyst[11] are often prepared via wet-chemical strategies such as hydrothermal synthesis or temperature-controlled reflux,[12,13] where molybdate and heating steps are required to control the structure and morphology of the products. The anodization of molybdenum metal in aqueous solution is generally unattainable because the anodization potential is higher than the oxidation of water and a stable and protective oxide film is formed on the surface of the electrode.[14-16] On the contrary, a blue MoO_x film was deposited on F-doped SnO_2 (FTO) film from a electrolyte of Na_2MoO_4 at different pHs and this could be related to the reduction of Mo^{VI} species[17]. The use of absolute ethanol would be a viable method to avoid the use of aqueous electrolytes or hydrated molybdate since the production of ionic species from ethanol under the microplasma would provide the charge carriers for the electrochemical reaction.[6,18]

Sensors are widely used in environmental monitoring, industrial/agricultural production and daily lives[19-21] and sensors based on nano-sized metal oxides, such as SnO_2, CeO_2 and perovskites, are popular ones for humidity sensing[22-25]. MoO_3 has been used in the humidity sensing of trimethylamine[26,27], ammonia[28], ethanol[29], volatile organic compounds (VOCs)[30,31] and hydrogen[17,31], but it can also be used for humidity sensing using the facile resistivity technique[32-38]. The α-MoO_3 based humidity sensor has been prepared via the evaporation of Mo^0 under an O_2 atmosphere[33,34] and MoO_3 plays a major role in enhancing the humidity sensing performance of composite due to the variation of microstructure[37] and the water adsorption kinetics in the composite sensor with oxides[32,34-36,38] of NiO, Cr_2O_3, WO_3 and *et al*. Mo^{VI} oxide in the highest oxidation state shows different crystalline phases depending on the synthetic routes[39-41]: four metastable phases have been reported for MoO_3 at high-temperature or high-pressure in addition to the stable orthorhombic 2-D α-MoO_3 phase[42,43]. For example, hexagonal molybdenum trioxide, a metastable phase that transforms to α-MoO_3 above 425 ^oC, has been reported to have a formula ranging from MoO_3 to $MoO_3.nH_2O$ ($0.09 \leq n \leq 0.69$) and allows a versatile intercalation chemistry with interesting chemical, electrochemical and catalytic properties[40,44,45]. The systematic study of the phase evolution of MoO_3 under different moisture and reducing/oxidation condition would benefit the design and understanding of humidity sensing.

In this study, we employed microplasma-assisted anodization of Mo metal to synthesize MoO_3 nanocrystals and the evolution of Mo species in anhydrous ethanol is examined over a period of two years to study the reduction and crystallization process. The anodization of Mo metal initially produces soluble Mo-oxyethoxide accompanied by a small fraction of Mo oxide crystals. These nanoparticles with diameters smaller than 10 nm are composed of

hexagonal nanocrystals with an orthorhombic domain structure on the edge. The soluble species are subjected to reduction for the production of blue polyoxometalates (POMs) after extended duration of aging at room temperature. The reducing agent for the POM clusters are the ethanol solvent being converted into ketones, but the addition of H_2O_2 to the initial suspension causes the formation of dendritic porous framework containing hexagonal crystallite. The direct anodization of Mo in an ionic-salt-free condition provides the exemplar situation for studying the evolution of Mo species in both solid and liquid phase under adjustable water content, advancing the understanding of inherent chemical steps during the synthesis of Mo-based functional materials for sensing the humidity and reducing/oxidizing species. The solid product from the suspension is also demonstrated to be steadily responsive to relative humidity (RH) in the range of 11% to 95%.

■ Experimental Section

■ *Preparation of the suspension:* A cultivation basin containing 20-mL absolute ethanol was used as the electrolytic tank and a graphite rod or a molybdenum bar was used as anode (**Figure S1)**. The depth of the Mo electrode was adjusted to give an immersed area of 5 cm^2. Helium gas passing through a nickel capillary was employed as the carrier gas of the microplasma for the cathode. The nickel capillary was 0.7 mm and 1.0 mm for inner and outer diameter, respectively, and the flow rate of He was 50 standard cubic centimeters per minute, sccm. The microplasma at the gas–solution interface initiated under a DC bias of 3 kV was stabilized by a ballast resistor of 100 kΩ. The anodization process at a constant current of 6.1 mA lasted over 40 min for the production of the suspension.

Characterization of the suspension: ^{1}H nuclear magnetic resonance (^{1}H NMR) of the

suspension/solution in $CDCl_3$ before and after the anodization process was recorded at 300.06 MHz (Bruker Advance 300, USA). Chemical shift of tetramethylsilane (TMS) was calibrated to be zero. An ultraviolet-visible (UV-Vis) light absorption spectroscopy of the suspension was recorded on a PerkinElmer Lambda 35 spectrometer equipped with an integrating sphere of 150-mm in diameter. Transmission electron microscopy (TEM) images and selective area electron diffraction (SAED) patterns were obtained using a field-emission electron microscope (JEM-2100F, JEOL, Japan) coupled with an energy dispersive spectroscopy (EDS). The accelerating voltage for the electron beam of TEM was adjusted to be 200 keV. A coating on glass or silicon single crystal was obtained by dripping 100 μL of the anodized solution on to the substrate, followed by a 5-hour drying in ambient air. The coatings were dried further at 60 °C for 1 hour or 250 °C for 30 minutes and then their superficial morphology is studied using scanning electron microscopy (SEM, 6700F, JEOL, Japan).

Characterization of the solid products: X-ray photoemission spectroscopy (XPS) of the dried coatings was carried out on a Kratos Axis Ultra XPS system equipped with a monochromatic X-ray with Al cathode (K_α=1468 eV). High-resolution core-level scans of Mo3d, O1s, C1s and valence band were recorded at a resolution of 0.05 eV. The recorded XPS data were calibrated by fixing the C 1s to be 284.5 eV. A Kelvin probe from KPtechnology was used to measure the Fermi level of the coatings on silicon and the values were calibrated against a gold reference. Powders of the solid product *via* the scratching of the dried coating were used for the Fourier transform infrared (FTIR) spectroscopy and thermo-gravimetric analysis (TGA). The FTIR was measured on a spectrometer

(Thermoscientific Nicolet iS5) with attenuated total reflection (ATR) accessory. TGA along with the simultaneous differential scanning calorimetry (DSC) in flowing synthetic air up to 800 °C was performed on an SDT Q600 (TA Instrument, USA).

Humidity sensing: For the humidity sensors, 1 μL suspension in ethanol was concentrated by drying in ambient air and dripping on to an interdigital electrode of gold coating. Multiple drippings followed by drying at 60 °C were used to increase the thickness of coating. The width of the gold coating (**Figure S2**) and blank space are 0.1 mm. Since different saturated salt solutions yield different relative humidity (RH) levels and thus the saturated solutions of LiCl (11% RH), $MgCl_2$ (33% RH), $Mg(NO_3)_2$ (53% RH), NaCl (75% RH), KCl (85% RH) and KNO_3 (95% RH) were used to control the RH[24,33]. The measurements were carried out by putting the samples into the columns with different RH levels while the direct-current (DC) conductivity was measured and recorded continuously using an electrochemical workstation (Zahner Pro, Zahner, Germany) at 18 °C.

■ Results and discussions

In the hybrid plasma-liquid systems, the auxiliary noble metal electrode that is normally used in a standard electrochemical cell is replaced by a gas-plasma electrode, and this overcomes the issue of dissolution of the noble metal at high overpotential, which is the cause of increased costs and sample contamination.[46] Hot electrons, ultraviolet photons and a localized higher temperature interface produced in the plasma process induce the production of radicals in solution for prolonged times that affect the production of crystals afterwards[47]. The soluble anodic product of the Mo^0 is Mo^{VI} in the form of molybdate or molybdic acid depending on to the pH of the solution because the oxide film of lower

valence could be a protective film on the surface[16,48,49]. Direct current anodization of Mo using LiCl electrolyte in ethanol under a bias above 110 V in dry box produced a red brown product of molybdenum oxyethoxide.[50] In our case, after the anodization of Mo with microplasma as counter electrode for 40 min, the absolute ethanol changed to a solution of yellowish color (**Figure 1(a)**) with the absorption edge around 450 nm (**Figure 1(A)**). However, a dramatic color change was found three weeks later for the samples encapsulated in a vial (**Figure 1(b)**); this blue solution can last for more than 2 years as long as good sealing of the vial is preserved (**Figure 1(c)**). The variation of color after the first three weeks is unnoticeable in a short period of time. The absorbance of the blue solution after three-week's ageing showed a broad peak at 721 nm in addition to the absorption band with an edge at 400 nm in the blue side of the spectrum, which is a clear indication of molybdenum blue[51]. The formation of blue species depends on the pH of the solution[40] : the solution should be acidic before and after the aging process[51]. After two-year aging in a sealed vial, the broad absorption that peaked at 721 nm in the sample after three weeks aging shifted its peak to 686 nm, which is linked to the acidification of the solution that causes further reduction of Mo^{VI} cations[52]. As the blue color is known to be from lone pair electron as in Mo^{V},[53] 5 vol.% H_2O_2 and H_2O were added to the yellowish solution (i.e. fresh samples) to explore the effect of electron acceptor and water content on the coloration of the solution. The addition of H_2O_2 changed instantly the original yellowish solution to a clear one (**Figure 1d**) and no blue product was found for the encapsulated solution in extended times (**Figure 1(e-f)**). The solution with H_2O_2 showed a blue-shifted absorption edge (**Figure 1D**) with respect to the fresh one (**Figure** 1A) and did not exhibit any broad absorption in the longer wavelength region. H_2O_2 is not only an oxidizing agent that could

be used to oxidize $MoO_{3-\delta}$ (δ is the oxygen deficiency) in aqueous solution under ambient conditions[54] but it is also a source of moisture for the solution; thus H_2O was also added to a yellowish colored fresh sample for comparison. The yellow tinge of the solution does not disappear instantly (**Figure 1g**) as in the case of H_2O_2 and no blue color was found after three weeks of aging as evidenced in the image of **Figure 1h**. However, a light blue product (**Figure 1i**) was finally observed after 24 months of aging and the absorption spectrum showed the broad absorption peaking at 711 nm, indicating that the addition of moisture does not prohibit the reduction of Mo^{VI} species[55]. Zhang et al. prepared the blue POM using aqueous solution from a molybdate with ascorbic acid as reducing agent and NaH_2PO_4 for the acidity[52], so it is reasonable to conclude that H_2O is not able to oxidize the Mo^{V}-containing species during the plasma process, but it does affect the formation process of molybdenum blue.

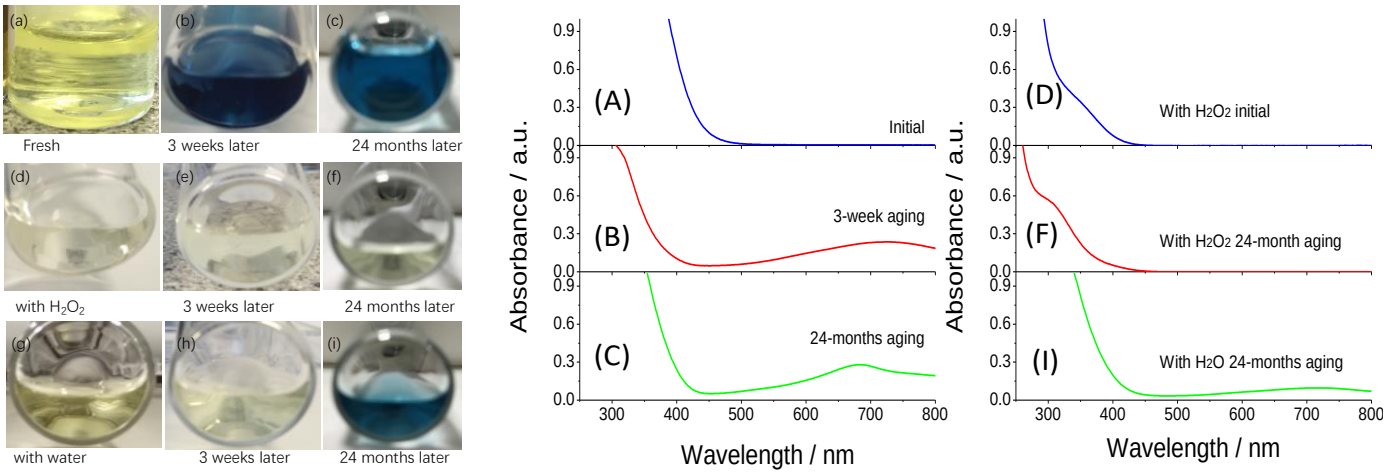

Figure 1. Digital image of the suspension of the pristine sample (a, b, c), H_2O_2 (d, e, f) and H_2O (g, h, i) treated suspension after the anodization under different aging times. Light absorbance of the presentative samples in a, b, c, d, f and I was shown in A, B, C, D, F and I, respectively.

^{1}H NMR spectra revealed that the samples had no observable singlet peak at a chemical shift of 1.56 ppm for free water molecules in a $CDCl_3$ solvent[56] (**Figure 2**). The anhydrous condition promotes the formation of ethyl acetate from ethanol with the graphite electrode (**Figure 2h**), while acetic acid is produced with Co anode under a high voltage[6]. In the case of Mo anode, a trace amount of acetic acid from NMR (**Figure S3**) for fresh and aged solution because molybdate is able to oxidize aldehyde into carboxylic acid[57]. Moreover, similar to the one with graphite anode (**Figure 2i**), formic acid was also found in the Mo-containing solution (**Figure 2c and f**) indicating that the process can break the C-C bonds, and thus the formation of $\bullet CH_3$ free radicals is possible. For the solutions with Mo species (Figure **2a and b**), an obvious change of the chemical shift to the high field was observed for the protons in $-CH_3$ and $-CH_2$ groups comparing to the original absolute ethanol, which indicates that ethanol and Mo species are forming a complexing bonding. The ^{1}H NMR of formic acid in the fresh anodized solution with Mo anode (**Figure 2a**) showed lower chemical shift by 0.08 ppm than the one with graphite anode (**Figure 2c**), indicating that they could also be connected to the Mo^{VI} cation. After the aging in a sealed vial, the protons in $-CH_2-$ and $-CH_3$ in the blue solution (inset of Figure **1b**) containing Mo^{V} showed larger chemical shift (**Figure 2a and b**) than the yellowish solution (**Figure 2d and e**) or pure ethanol (**Figure 2j and k**) which could be explained by the lower electronegativity of Mo^{V} than Mo^{VI} causing the reduction of electron density around the protons. A enlarged image of the NMR in **Figure 2b** shows a set of peaks with chemical shift of 2.46 ppm and 2.17 ppm, which could be assigned to the formation of acetone and/or ethyl methyl ketone in the suspension[56]. Though a plasma is well known to produce long-lived radicals and electrons which could act as the reducing agents for the Mo^{VI} species, the reducing agent could be the

ethoxide ligand on Mo^{VI} via discoordination and formation of ketones for the reactions that take on after a duration as long as three weeks.[53,57] Commercially available yellow bis(acetylacetonate)dioxomolybdenum(VI) ($MoO_2(acac)_2$) is reported to gradually convert to molybdenum blue (MB) in cyclohexanol solvent as reducing agent[53]. Therefore a similar mechanism of reduction could be written briefly as[53]:

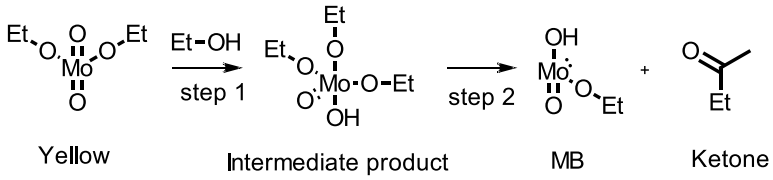

(1)

where Et denotes an ethyl group. H_2O would compete with EtOH to combine with the yellow intermediate product in step 1 or drive the reaction to the left side in step 2, and thus retards the formation of MB. Nonetheless, the addition of water did not prohibit the formation of MB as long as the sample is aged for a duration as long as 2 years.

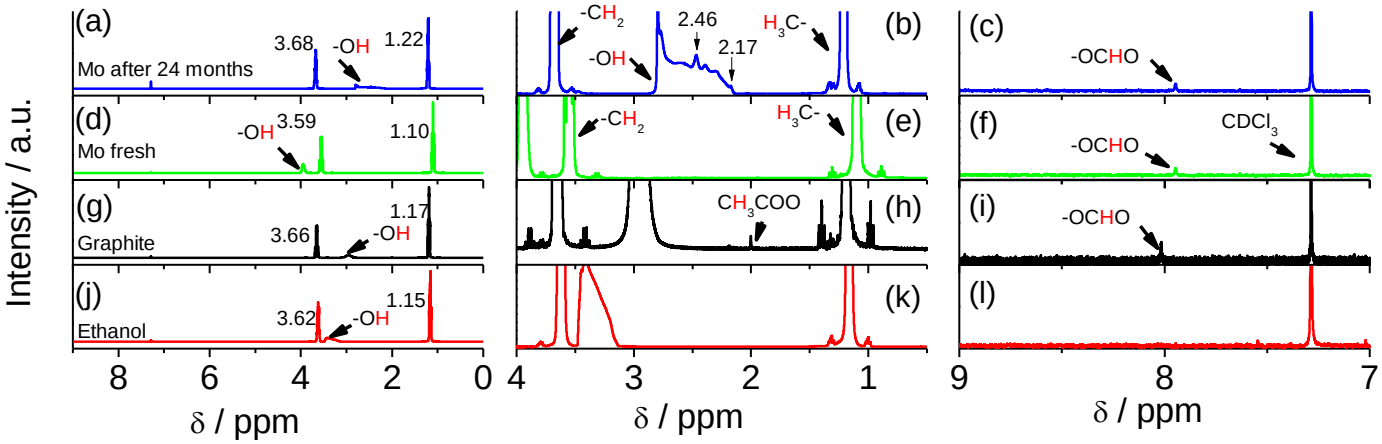

Figure 2. ^1H NMR of suspension in $CDCl_3$ after the anodization with graphite cathode and Mo^0 anode. The limiting currents for Mo and graphite anode are 6.1 mA and 4.6 mA, respectively. The spectrum of pure ethanol was provided for comparison and the central position of the chemical shifts for proton in $-CH_3$ and $-CH_2$ was indicated in (a). The NMR

spectra for suspension with Mo (d, e, f) and graphite (g, h, i) are presented at different scales. Similarly, the spectra for pure ethanol (j, k, l) and the aged Mo suspension after 24 months (a, b, c) were shown for comparison.

When Mo is anodized in ethanol, some of the Mo species will be transported into ethanol to interact with the plasma cathode and liquid media. Solid particles were observed in the transmission electron microscopy (TEM) analysis (**Figure 3**). Most of the particles are well-dispersed crystals with diameters of less than 10 nm (Figure 3(a)); a close-up image (Figure 3(b)) of the nanocrystals revealed that there are quite a few domains. The nanoparticles are generally in hexagonal symmetry and the *d*-spacings are in agreement with hexagonal MoO_3 as shown in Figure 3(b), though we are not clear about the actual water content in the lattice. The interaction of plasma and ambient air is known to reduce the pH of the solution because of the formation of trace NO_x and H_2O_2 that acidifies the solution.[58] The local anhydrous environment also causes the formation of α-MoO_3 on the edge of the particles as shown in the higher-magnification images in **Figure 3**(b, c). It should be noted that the hexagonal and orthorhombic phase shares the crystal planes during the phase transition process and the *d*-spacings for (300) planes in the former is identical to that for (200) plane in the latter.

Mo species in a reduced form can be also engineered in electron-rich POMs of different archetypes, structural flexibilities and functionalities.[40,55] The valence reduction of Mo^{VI} in MoO_3 under mild reduction environment in colloid systems can bring about the color change and electronic structure variation in both solid and solution conditions[51]. The reduction of Mo^{VI} species by Mohr's salt, ethanol, formic acid and $SnCl_2$ et al. can produce

the well-known molybdenum blue (MB) in acidic conditions containing giant POM clusters (on the scale of 1 nm to 100 nm) through the crystallization and precipitation process.[55] Reduced molybdenum species with lone pair electrons on Mo cation showing brilliant colors can absorb H_2O or other small molecules as ligands and can be used for the clinical agent or clock reactions due to its special photothermal properties.[52,53] The TEM image of the blue sample (**Figure 3**(d)) showed that Mo species grew up to beads larger than 200 nm after three weeks. Some of the large clusters are hollow in the middle as can be seen from the broken particles (**Figure 3**(d)) as a result of the electron-doping and linking ligand assisting for formation of amphiphilic O=MoL (L= small molecular ligands)[51] that promoted the ring-shaped supramolecular clusters[51]. These giant clusters precipitated as the amount of Mo^V species exceeded its solubility in ethanol and formed suspended particles and the hollow structure is attractive due to the special properties in many applications[44]. The detailed high-resolution imaging of the structure of the blue precipitate is very difficult because it suffers structure change under the electron beam, which could be related to the evaporation of small molecules, such as ethanol, formic acid etc., adsorbed in the giant structure. However, we can determine from the TEM image that the intact beads showed that defective domains of α-MoO_3 can be determined after the annealing under electron beam (**Figure 3**(e, f)). The formation of defective domains and structure change can be related to the loss of small molecule ligands under the electron beam.

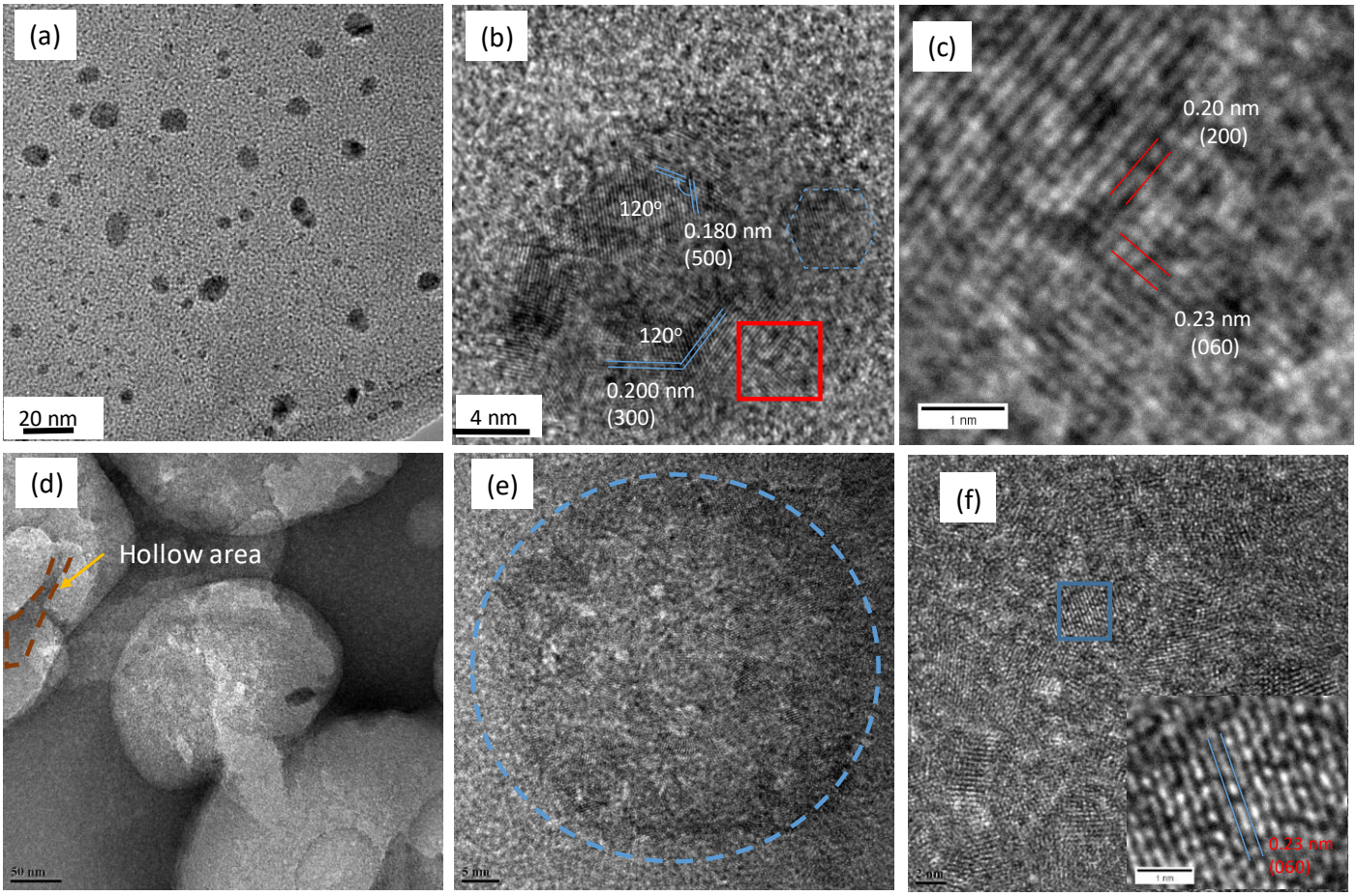

Figure 3. TEM images of the nanocrystals from the fresh (a, b, c) and aged blue suspension (d, e, f) under different magnifications. The *d*-spacings and angles in (b) belongs to hexagonal MoO_3. (c) shows the higher-magnification image in the rectangle in (b). (d) is the low-magnification of the blue sample after three weeks of aging in capsulated vial and (e) shows the effect of electron beam on the structure of particles. (f) is a higher-magnification image of the electron-beam annealed area. The inset in (f) shows the magnified image in the blue rectangle in (f).

The addition of H_2O_2 changed dramatically the morphology of the particles in the products. H_2O_2 caused the re-crystallization of the Mo species as can be seen from the sharp edges and crystal aggregation in the TEM image (**Figure 4**(a, b)); EDS analysis (**Figure S4**) verified that Mo species are contained for the most part. The fine crystalline particles

are composed of both hexagonal and orthorhombic MoO_3 crystals (**Figure 4(b)**), but the two phases are less likely to form a montage of crystals. After three weeks of aging, the quantity of crystalline phases increased significantly and formed a dendritic framework as shown in **Figure 4** (c, d) and the detailed imaging of a single particles showed a hexagonal structure (**Figure 4(e)**). The detail imaging and the corresponding SAED pattern **(Figure 4 (d, f))** showed that this framework was composed mostly of *h*-MoO_3 crystallite and on the scale of 20 nm in diameter. These observations indicate that the instant reaction between H_2O_2 and the Mo species are in the liquid phase after the addition of H_2O_2 since the reaction in solid state would require long distance diffusion of ions and extended times, but it will affect the production of Mo particles afterwards.

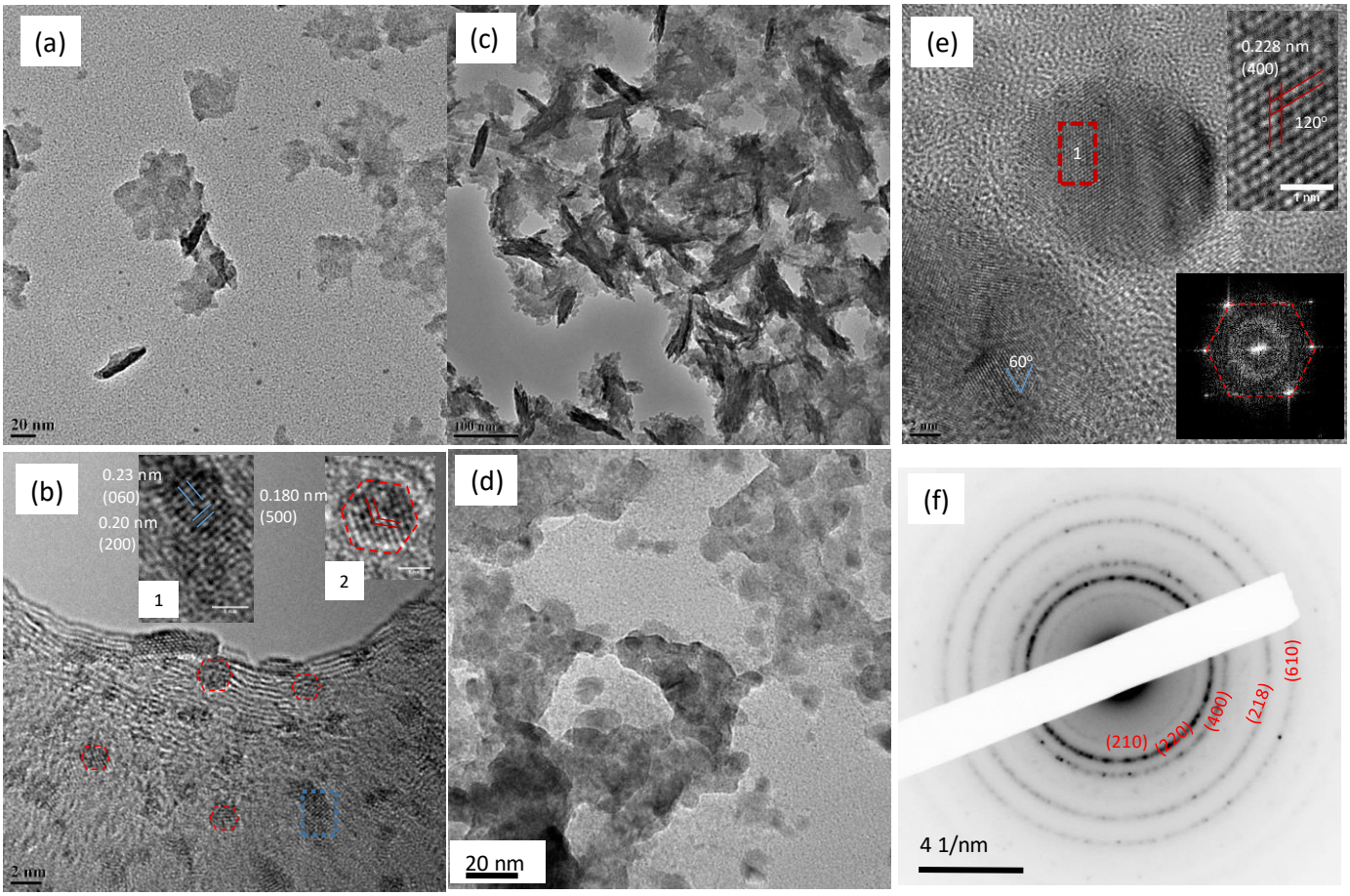

Figure 4. TEM images of the nanocrystals from the fresh (a, b) and aged (c, d, e)

suspension with H_2O_2. The inset 1 in (b) shows the higher-magnification image in the blue rectangle while inset 2 shows the magnified image in the red hexagon. FFT transformation was done on round crystal at the center in (e) and the magnified image in red rectangle is shown as inset as well. (f) shows SAED image of (d).

As the Mo species could form complexes with ethanol, water molecules and other small molecules that were produced during the plasma-assisted anodization, the weight of these ligands were analyzed using simultaneous thermogravimetric analysis (TGA) and differential scanning calorimetry (DSC) under an air atmosphere **(Figure 5)**. The weight loss of the sample with a pre-drying in air at 80 °C loses 24% of the total weight up to 500 °C. The decomposition of  to MoO_3 would be expected to induce a theoretical weight loss of 34.5% and the lower weight loss in our TGA could be explained by the initial prior weight loss incurred when the sample was dried at 80 °C. An obvious endothermic peak with a simultaneous derivative thermogravimetric peak was observed at 422 °C, which is very close to the phase transition temperature (425 °C[40]) between the hexagonal to orthorhombic MoO_3.[59] The weight gain at 486 °C could be the oxygenation of the oxide after the fully de-coordination of organic groups[60]. At temperatures higher than 650 °C, the oxides start to lose weight due to the formation of oxygen vacancies.

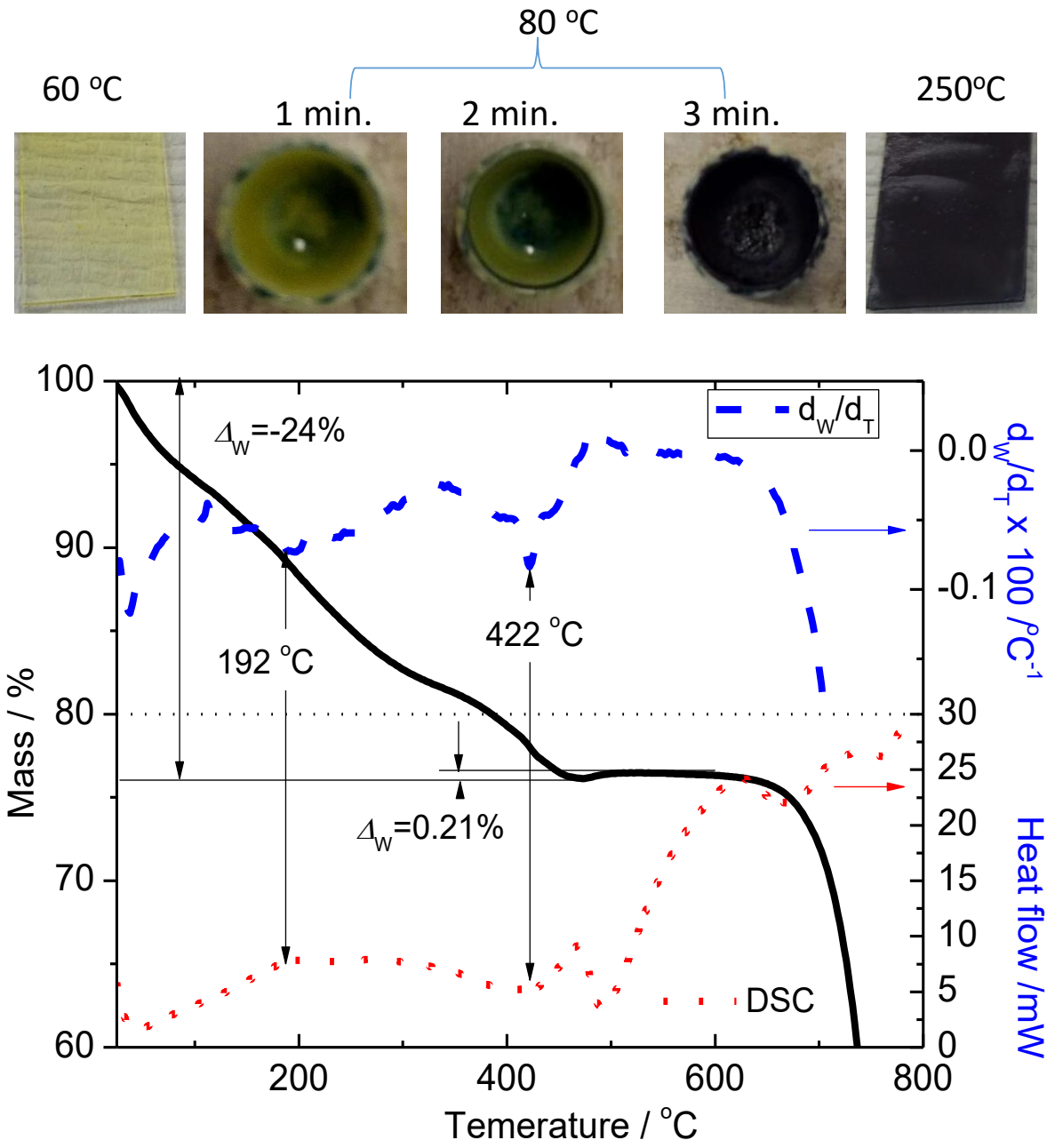

Figure 5. Simultaneous TGA and DSC curves in flowing air (a) for the powders after the drying at 80 °C for 0.5 hour in the ambient air. The images above the TGA curves shows the color variation of the suspension/solid product at different temperatures and annealing times at 80 °C.

Molybdenum oxides can be processed to dense coatings, dispersed nanoparticles/plates

or mesoporous frameworks for energy applications[59,61-64]. The kinetics for the formation of Mo^{V} species in the photothermal reaction depends on temperature and the concentration of Mo species in the solution.[53] The fresh suspension underwent color change very quickly at 80 °C and turn out to be dark brown after 3 minutes as can be seen from the images in **Figure 5**. Scanning electron microscopy (SEM) of the dark brown film formed at 80 °C on glass (**Figure S5**) showed a dense surface, while the growth of first-order hierarchical structures can be achieved via the anneal of mixture of ammonium molybdate and citrate acid as a meditator[65] or chemical vapor deposition (CVD)[66]. The initial yellow film with a bandgap of 2.68 eV as indicated in the Tauc plot in **Figure S6** turn into a dark brown one showing high absorption even in the NIR region after the calcination at 250 °C (**Figure S6**). The strong absorption at 900 nm could be explained by the intermediate electronic state near the Fermi level as in the X-ray photoemission spectroscopy (XPS) valence band (**Figure 6**) due to the formation of Mo^{V} and the oxygen vacancies [67] since the conduction band of MoO_3 is dominated by Mo d states with some hybridization with O 2p states[68]. Mo^{V} accounts for 20% of the Mo cations after the calcination at 250 °C by comparing the deconvoluted area for Mo^{V} and Mo^{VI} in the Mo 3d spectra. MoOx crystals were synthesized hydrothermally using H_2MoO_4 in the presence of polyethylene glycol (PEG) and found that the presence of 100 g/L PEG induces spherical crystals containing Mo^{V} and Mo^{IV}.[69] Although the product has not been converted fully into oxides at temperature lower than 250 °C, the work function (**Figure S7**) of the coating is in the range between -5.06 and -5.24 eV, which is close to the air-exposed MoO_3 (-5.3 eV).[70] As a typical *n* type semiconductor, the Fermi level could be close to the minimum of conduction band and the rising of density of state near the Fermi level would not induce major change to the Fermi level. The FTIR spectrum

(**Figure S8**) of the fresh suspension dried at 60 °C showed clear absorption peaks for vibrations of Mo=O (977 and 911 cm^{-1}) and Mo-O (below 650 cm^{-1}) bonds[13], but the one for oxygen stretching in Mo-O-Mo (860 cm^{-1}) presented as a shoulder to the one at 911 cm^{-1}. This indicates that the product of anodization is molybdenum oxyethoxide rather than pure ethoxide after the anodization process. The presence of ethoxide anion could also explain the lower binding energy and smaller h for the Mo^{VI} in Mo60 and Mo250 due to the loss of ethoxide in the latter. After the thermal treatment at 250 °C, the peak at 911 cm^{-1} for Mo=O bond disappeared but is replaced by a wide peak below 930 cm^{-1}, which could be ascribed to the vibration of oxygen atom linking multiple Mo atoms after the loss of organics and the formation Mo-O-Mo bonds. More importantly, an obvious broad peak for OH group at 3400 cm^{-1} was found in the sample dried at 60 °C, clearly indicates the interaction between the water molecules and the MoO_3 oxides.

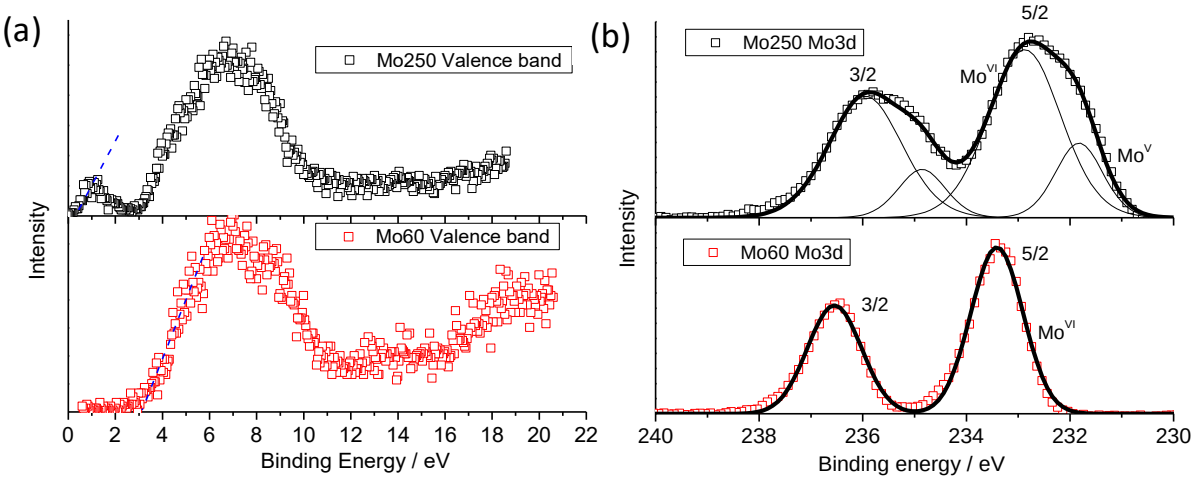

Figure 6. XPS of the coating after drying at 60 °C (denoted as Mo60) and 250 °C (denoted as Mo250): valence band (a), and Mo 3d (b).

As can be seen from the aforementioned study, the structure of MoO_3 can be affected by thermal treatment and water molecules, so a thin film interdigital electrode was

employed to study the humidity sensing properties. The electric resistivity, σ, of the electrode is affected significantly by the variation of relative humidity, RH, **(Figure 7)** and a linear plot can be achieved in the plot of humidity versus Log(σ). The response time at 95% relative humidity for examples takes only 10 seconds while the recovery times are less than 3 seconds, which is comparable to nanocrystalline CeO_2 as humidity sensor[25] but is shorter than MoO_3 film from CVD technique (60 seconds to respond and 5 seconds to recover[33]). The increase of conductivity with humidity on ceramic sensors is attributed to the adsorption of water molecules on the defect site of the oxides[23], generating a proton conductivity. In the suspension containing nanocrystals Mo^{VI} species, the absorbed water molecules can be dissociated to give an increased proton conductivity:

$$2H_2O = H_3O^+ + OH^- \quad (2)$$

The adsorption of water molecules can be evidenced by the FTIR and the result is consistent with the observation of hexagonal MoO_3 containing water molecules in the TEM. Chithambararaj *et al.* [71] studied the electric properties of *h*-MoO_3 and α-MoO_3 and found that the former could show superionic conductance under the condition of water or ammonia molecules.

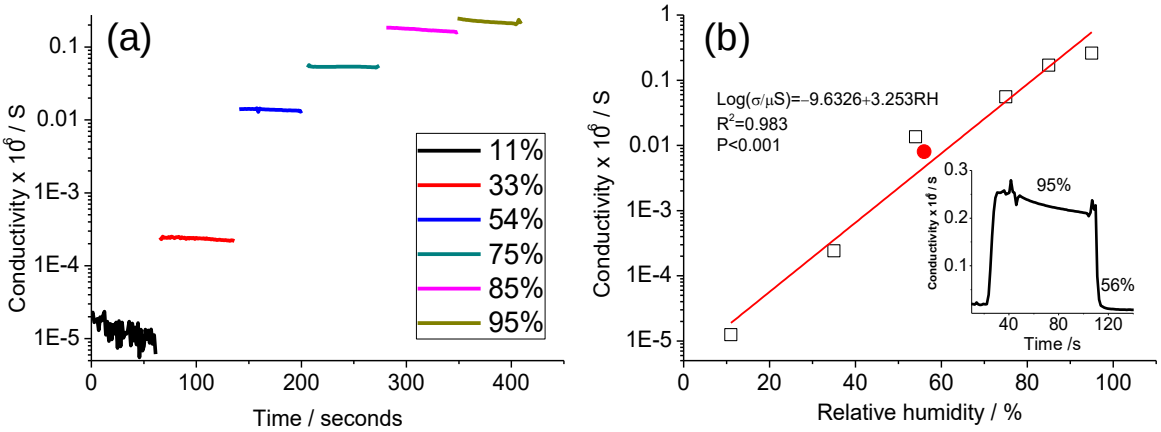

Figure 7. Conductivity variation under different relative humidity at 18 ^{o}C (a) and plot of log(σ) versus relative humidity, RH. (b). The red dot in (b) shows the resistivity and relative humidity in ambient air and the inset represent a typical response and recovery cycle.

■ Conclusion

Molybdenum metal (Mo^{0}) was anodized in pure ethanol electrolyte at high voltage with a gaseous microplasma electrode in ambient conditions. The product shortly after the synthesis process is mostly Mo oxyethoxide, which is soluble in ethanol solvent. However small amounts of MoO_3 crystals containing mixed hexagonal and orthorhombic phases were produced and the (300) planes in the former share the (200) ones in the latter. Ethanol is the reducing agent for the transition between Mo^{VI} to Mo^{V} cation with lone pair electrons and ethanol molecules can also be the small molecules absorbing on the Mo^{V} to form POMs. The oxidation of ethanol in our case produces ketone rather than aldehyde or carboxylate. In addition, water is critically important to the reduction kinetics of Mo^{V} while H_2O_2 is able to promote a dendritic framework of hexagonal MoO_3 crystallite. The light absorbance of the coating varies with the thermal treatment at 250 ^{o}C and midgap states evolved and this could increase the conductivity of the solids. The coating can be used for humidity sensing based on facile electric conductivity measurement because of the (de-)adsorption of water molecules affecting the protonic conduction at 18 ^{o}C. The study of crystal evolution of MoO_3 species under water, ethanol and H_2O_2 would benefit the design and understanding of sensing of different gases.

■ Acknowledgements

We would like to thank the support from National Natural Science Foundation of China (NSFC, 51702264; 41371275), Fundamental Research Funds for the Central Universities (XDJK2017B033) and Research Funding of Southwest University (SWU117019). The funding from the Engineering and Physical Sciences Research Council (EPSRC) under the grant number EP/K022237/1, EP/K036769/1, EP/M024938/1 is also acknowledged. We also appreciate the Funding from the EU COST Action TD1208 for useful exchanges and discussions. We also thank Ms. Zhang Ziye from Southwest University for the measurement of conductivity under different relative humidity.

Graphical abstract

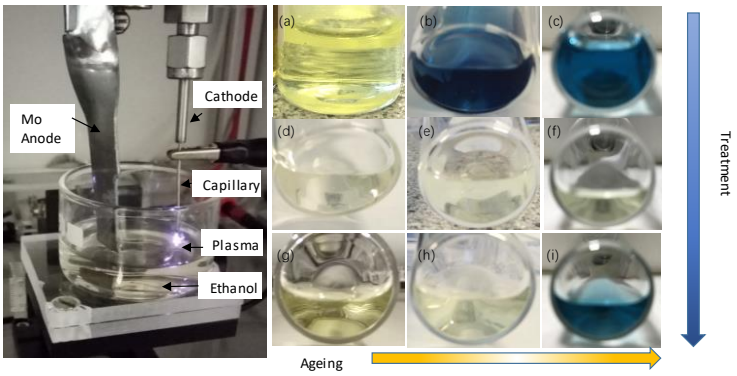

Microplasma-assisted anodization is employed to prepare soluble and crystalline Mo species in a water-deficient and extraneous ionic-salt-free ethanol electrolyte and the crystal growth and properties of the resultant Mo species were observed and used for humidity sensing.

Reference

(1) Pinna, N.; Niederberger, M. Surfactant-Free Nonaqueous Synthesis of Metal Oxide Nanostructures. *Angew. Chem. Int. Ed.* **2008**, *47*, 5292-5304.

(2) Cheng, F.; Shen, J.; Peng, B.; Pan, Y.; Tao, Z.; Chen, J. Rapid room-temperature synthesis of nanocrystalline spinels as

oxygen reduction and evolution electrocatalysts. *Nat Chem* **2011**, *3*, 79-84.

(3) Welton, T. Room-Temperature Ionic Liquids. Solvents for Synthesis and Catalysis. *Chem. Rev. (Washington, DC, U. S.)* **1999**, *99*, 2071-2084.

(4) Maguire, P.; Rutherford, D.; Macias-Montero, M.; Mahony, C.; Kelsey, C.; Tweedie, M.; Pérez-Martin, F.; McQuaid, H.; Diver, D.; Mariotti, D. Continuous In-Flight Synthesis for On-Demand Delivery of Ligand-Free Colloidal Gold Nanoparticles. *Nano Lett.* **2017**, *17*, 1336-1343.

(5) Wang, R.; Zuo, S.; Wu, D.; Zhang, J.; Zhu, W.; Becker, K. H.; Fang, J. Microplasma-Assisted Synthesis of Colloidal Gold Nanoparticles and Their Use in the Detection of Cardiac Troponin I (cTn-I). *Plasma Processes Polym.* **2015**, *12*, 380-391.

(6) Ni, C.; Carolan, D.; Rocks, C.; Hui, J.; Fang, Z.; Padmanaban, D. B.; Ni, J.; Xie, D.; Maguire, P.; Irvine, J. T. S.; Mariotti, D. Microplasma-assisted electrochemical synthesis of Co_3O_4 nanoparticles in absolute ethanol for energy applications. *Green Chem.* **2018**, *20*, 2101-2109.

(7) Velusamy, T.; Liguori, A.; Macias-Montero, M.; Padmanaban, D. B.; Carolan, D.; Gherardi, M.; Colombo, V.; Maguire, P.; Svrcek, V.; Mariotti, D. Ultra-small CuO nanoparticles with tailored energy-band diagram synthesized by a hybrid plasma-liquid process. *Plasma Processes Polym.* **2017**, 1600224.

(8) Du, C.; Xiao, M. Cu_2O nanoparticles synthesis by microplasma. *Sci. Rep.* **2014**, *4*, 7339.

(9) Senthilnathan, J.; Weng, C.-C.; Liao, J.-D.; Yoshimura, M. Submerged Liquid Plasma for the Synthesis of Unconventional Nitrogen Polymers. *Sci. Rep.* **2013**, *3*, 2414.

(10) Carolan, D.; Rocks, C.; Padmanaban, D. B.; Maguire, P.; Svrcek, V.; Mariotti, D. Environmentally friendly nitrogen-doped carbon quantum dots for next generation solar cells. *Sustainable Energy & Fuels* **2017**, *1*, 1611-1619.

(11) Stubhan, T.; Ameri, T.; Salinas, M.; Krantz, J.; Machui, F.; Halik, M.; Brabec, C. J. High shunt resistance in polymer solar cells comprising a MoO_3 hole extraction layer processed from nanoparticle suspension. *Appl. Phys. Lett.* **2011**, *98*.

(12) Lou, X. W.; Zeng, H. C. Complex alpha-MoO_3 nanostructures with external bonding capacity for self-assembly. *J. Am. Chem. Soc.* **2003**, *125*, 2697-2704.

(13) Wongkrua, P.; Thongtem, T.; Thongtem, S. Synthesis of h- and alpha-MoO_3 by Refluxing and Calcination Combination: Phase and Morphology Transformation, Photocatalysis, and Photosensitization. *J. NANOMATER.* **2013**.

(14) Knorr, K.; Leslie, J. D. Plasma anodization of titanium and molybdenum. *Thin Solid Films* **1974**, *23*, 101-107.

(15) Ikonopisov, S. Electrolytes for anodization of molybdenum. *Electrodeposition and Surface Treatment* **1974**, *2*, 411-418.

(16) Badawy, W. A.; Gad-Allah, A. G.; Abd El-Rahman, H. A.; Abou-Romia, M. M. On the stability of anodic oxide films formed on molybdenum in various aqueous solutions. *Surf. Coat. Technol.* **1987**, *30*, 365-373.

(17) Di Yao, D.; Ou, J. Z.; Latham, K.; Zhuiykov, S.; O'Mullane, A. P.; Kalantar-zadeh, K. Electrodeposited alpha- and beta-Phase MoO3 Films and Investigation of Their Gasochromic Properties. *Cryst. Growth Des.* **2012**, *12*, 1865-1870.

(18) Chen, Q.; Kitamura, T.; Saito, K.; Haruta, K.; Yamano, Y.; Ishikawa, T.; Shirai, H. Microplasma discharge in ethanol solution: Characterization and its application to the synthesis of carbon microstructures. *Thin Solid Films* **2008**, *516*, 4435-4440.

(19) Lv, C.; Hu, C.; Luo, J.; Liu, S.; Qiao, Y.; Zhang, Z.; Song, J.; Shi, Y.; Cai, J.; Watanabe, A. Recent Advances in Graphene-Based Humidity Sensors. *Nanomaterials (Basel, Switzerland)* **2019**, *9*.

(20) Kuang, Q.; Lao, C.; Wang, Z. L.; Xie, Z.; Zheng, L. High-Sensitivity Humidity Sensor Based on a Single SnO2 Nanowire. *J. Am. Chem. Soc.* **2007**, *129*, 6070-6071.

(21) Lu, T.; Song, H. J.; Dong, X. Q.; Hu, J. Y.; Lv, Y. A highly selective and fast-response photoluminescence humidity sensor based on F- decorated NH2-MIL-53(Al) nanorods. *J. Mater. Chem. C* **2017**, *5*, 9465-9471.

(22) Shimizu, Y.; Shimabukuro, M.; Arai, H.; Seiyama, T. Humidity ‐ Sensitive Characteristics of La3+ ‐ Doped and Undoped SrSnO3. *J. Electrochem. Soc.* **1989**, *136*, 1206-1210.

(23) Traversa, E. Ceramic sensors for humidity detection: the state-of-the-art and future developments. *Sens. Actuator B-Chem.* **1995**, *23*, 135-156.

(24) Li, M.; Chen, X. L.; Zhang, D. F.; Wang, W. Y.; Wang, W. J. Humidity sensitive properties of pure and Mg-doped CaCu3Ti4O12. *Sens. Actuator B-Chem.* **2010**, *147*, 447-452.

(25) Xie, W.; Liu, B.; Xiao, S.; Li, H.; Wang, Y.; Cai, D.; Wang, D.; Wang, L.; Liu, Y.; Li, Q.; Wang, T. High performance humidity sensors based on CeO2 nanoparticles. *Sens. Actuator B-Chem.* **2015**, *215*, 125-132.

(26) Yang, S.; Liu, Y.; Chen, W.; Jin, W.; Zhou, J.; Zhang, H.; Zakharova, G. S. High sensitivity and good selectivity of ultralong MoO3 nanobelts for trimethylamine gas. *Sens. Actuator B-Chem.* **2016**, *226*, 478-485.

(27) Pandeeswari, R.; Jeyaprakash, B. G. Nanostructured alpha-MoO3 thin film as a highly selective TMA sensor. *Biosens. Bioelectron.* **2014**, *53*, 182-186.

(28) Guentner, A. T.; Righettoni, M.; Pratsinis, S. E. Selective sensing of NH3 by Si-doped alpha-MoO3 for breath analysis. *Sens. Actuator B-Chem.* **2016**, *223*, 266-273.

(29) Wang, L.; Gao, P.; Bao, D.; Wang, Y.; Chen, Y.; Chang, C.; Li, G.; Yang, P. Synthesis of Crystalline/Amorphous Core/Shell MoO3 Composites through a Controlled Dehydration Route and Their Enhanced Ethanol Sensing Properties. *Cryst. Growth Des.* **2014**, *14*, 569-575.

(30) Arachchige, H. M. M. M.; Zappa, D.; Poli, N.; Gunawardhana, N.; Comini, E. Gold functionalized MoO3 nano flakes for gas sensing applications. *Sens. Actuator B-Chem.* **2018**, *269*, 331-339.

(31) Illyaskutty, N.; Kohler, H.; Trautmann, T.; Schwotzer, M.; Pillai, V. P. M. Hydrogen and ethanol sensing properties of molybdenum oxide nanorods based thin films: Effect of electrode metallization and humid ambience. *Sens. Actuator B-Chem.* **2013**, *187*, 611-621.

(32) Li, D.; Li, Y.; Li, F.; Zhang, J.; Zhu, X.; Wen, S.; Ruan, S. Humidity sensing properties of MoO3-NiO nanocomposite materials. *Ceram. Int.* **2015**, *41*, 4348-4353.

(33) Jadkar, V.; Pawbake, A.; Waykar, R.; Jadhavar, A.; Mayabadi, A.; Date, A.; Late, D.; Pathan, H.; Gosavi, S.; Jadkar, S. Synthesis of orthorhombic-molybdenum trioxide (alpha-MoO3) thin films by hot wire-CVD and investigations of its humidity sensing properties. *Journal of Materials Science-Materials in Electronics* **2017**, *28*, 15790-15796.

(34) Kim, H.-U.; Son, J.; Kulkarni, A.; Ahn, C.; Kim, K. S.; Shin, D.; Yeom, G. Y.; Kim, T. Highly uniform wafer-scale synthesis of alpha-MoO3 by plasma enhanced chemical vapor deposition. *Nanotechnology* **2017**, *28*.

(35) Pokhrel, S.; Nagaraja, K. S. Solid state electrical conductivity and humidity sensing properties of Cr_2O_3-MoO_3 composites. *Physica Status Solidi a-Applications and Materials Science* **2002**, *194*, 140-146.

(36) Pokhrel, S.; Nagaraja, K. S. Electrical and humidity sensing properties of molybdenum(VI) oxide and tungsten(VI) oxide composites. *Physica Status Solidi a-Applied Research* **2003**, *198*, 343-349.

(37) Reddy, L. P. B.; Megha, R.; Chethan, B.; Prakash, H. G. R.; Ravikiran, Y. T.; Ramana, C. H. V. V.; Kim, D. Role of molybdenum trioxide in enhancing the humidity sensing performance of magnesium ferrite/molybdenum trioxide composite. *Inorg. Chem. Commun.* **2018**, *98*, 68-74.

(38) Sundaram, R.; Nagaraja, K. S. Solid state electrical conductivity and humidity sensing studies on metal molybdate-molybdenum trioxide composites (M = Ni2+Cu2+ and Pb2+). *Sens. Actuator B-Chem.* **2004**, *101*, 353-360.

(39) Lunk, H.-J.; Hartl, H.; Hartl, M. A.; Fait, M. J. G.; Shenderovich, I. G.; Feist, M.; Frisk, T. A.; Daemen, L. L.; Mauder, D.; Eckelt, R.; Gurinov, A. A. "Hexagonal Molybdenum Trioxide"—Known for 100 Years and Still a Fount of New Discoveries. *Inorg. Chem.* **2010**, *49*, 9400-9408.

(40) Zheng, L.; Xu, Y.; Jin, D.; Xie, Y. Novel Metastable Hexagonal MoO3 Nanobelts: Synthesis, Photochromic, and Electrochromic Properties. *Chem. Mater.* **2009**, *21*, 5681-5690.

(41) Sakaushi, K.; Thomas, J.; Kaskel, S.; Eckert, J. Aqueous Solution Process for the Synthesis and Assembly of Nanostructured One-Dimensional alpha-MoO_3 Electrode Materials. *Chem. Mater.* **2013**, *25*, 2557-2563.

(42) Hu, X. K.; Qian, Y. T.; Song, Z. T.; Huang, J. R.; Cao, R.; Xiao, J. Q. Comparative study on MoO3 and HxMoO3 nanobelts: Structure and electric transport. *Chem. Mater.* **2008**, *20*, 1527-1533.

(43) Ren, H.; Sun, S.; Cui, J.; Li, X. Synthesis, Functional Modifications, and Diversified Applications of Molybdenum Oxides Micro-/Nanocrystals: A Review. *Cryst. Growth Des.* **2018**, *18*, 6326-6369.

(44) Mariotti, D.; Lindström, H.; Bose, A. C.; Ostrikov, K. K. Monoclinic β-MoO_3 nanosheets produced by atmospheric microplasma: application to lithium-ion batteries. *Nanotechnology* **2008**, *19*, 495302.

(45) Kiebach, R.; Pienack, N.; Bensch, W.; Grunwaldt, J. D.; Michailovski, A.; Baiker, A.; Fox, T.; Zhou, Y.; Patzke, G. R. Hydrothermal formation of W/Mo-Oxides: A multidisciplinary study of growth and shape. *Chem. Mater.* **2008**, *20*, 3022-3033.

(46) Richmonds, C.; Witzke, M.; Bartling, B.; Lee, S. W.; Wainright, J.; Liu, C.-C.; Sankaran, R. M. Electron-Transfer Reactions at the Plasma–Liquid Interface. *J. Am. Chem. Soc.* **2011**, *133*, 17582-17585.

(47) Mariotti, D.; Švrček, V.; Hamilton, J. W. J.; Schmidt, M.; Kondo, M. Silicon Nanocrystals in Liquid Media: Optical Properties and Surface Stabilization by Microplasma-Induced Non-Equilibrium Liquid Chemistry. *Adv. Funct. Mater.* **2012**, *22*, 954-964.

(48) Mahadevaiah, N.; Venkataramani, B.; Prakash, B. S. J. Restrictive entry of aqueous molybdate species into surfactant modified montmorillonite - A breakthrough curve study. *Chem. Mater.* **2007**, *19*, 4606-4612.

(49) Pereira, A. C.; Ferreira, T. L.; Kosminsky, L.; Matos, R. C.; Bertotti, M.; Tabacniks, M. H.; Kiyohara, P. K.; Fantini, M. C. A. Characterization of electrochemically co-deposited metal-molybdenum oxide films. *Chem. Mater.* **2004**, *16*, 2662-2668.

(50) Kessler, V. G.; Panov, A. N.; Turova, N. Y.; Starikova, Z. A.; Yanovsky, A. I.; Dolgushin, F. M.; Pisarevsky, A. P.; Struchkov, Y. T. Anodic oxidation of molybdenum and tungsten in alcohols: isolation and X-ray single-crystal study of side products. *J. Chem. Soc. Dalton Trans.* **1998**, 21-30.

(51) Müller, A.; Serain, C. Soluble Molybdenum Blues"des Pudels Kern". *Acc. Chem. Res.* **2000**, *33*, 2-10.

(52) Zhang, C.; Bu, W. B.; Ni, D. L.; Zuo, C. J.; Cheng, C.; Li, Q.; Zhang, L. L.; Wang, Z.; Shi, J. L. A Polyoxometalate Cluster Paradigm with Self-Adaptive Electronic Structure for Acidity/Reducibility-Specific Photothermal Conversion. *J. Am. Chem. Soc.* **2016**, *138*, 8156-8164.

(53) Neuenschwander, U.; Negron, A.; Jensen, K. F. A Clock Reaction Based on Molybdenum Blue. *J. Phys. Chem. A* **2013**, *117*, 4343-4351.

(54) Sharma, A. K.; Pandey, S.; Sharma, K. H.; Nerthigan, Y.; Khan, M. S.; Hang, D. R.; Wu, H. F. Two dimensional alpha-MoO3-x nanoflakes as bare eye probe for hydrogen peroxide in biological fluids. *Anal. Chim. Acta* **2018**, *1015*, 58-65.

(55) Gumerova, N. I.; Rompel, A. Synthesis, structures and applications of electron-rich polyoxometalates. *Nat. Rev. Chem.* **2018**, *2*.

(56) Gottlieb, H. E.; Kotlyar, V.; Nudelman, A. NMR chemical shifts of common laboratory solvents as trace impurities. *J. Org. Chem.* **1997**, *62*, 7512-7515.

(57) Trost, B. M.; Masuyama, Y. Chemoselectivity in molybdenum catalyzed alcohol and aldehyde oxidations. *Tetrahedron Lett.* **1984**, *25*, 173-176.

(58) Rumbach, P.; Witzke, M.; Sankaran, R. M.; Go, D. B. Decoupling Interfacial Reactions between Plasmas and Liquids: Charge Transfer vs Plasma Neutral Reactions. *J. Am. Chem. Soc.* **2013**, *135*, 16264-16267.

(59) Epifani, M.; Imperatori, P.; Mirenghi, L.; Schioppa, M.; Siciliano, P. Synthesis and characterization of MoO3 thin films and powders from a molybdenum chloromethoxide. *Chem. Mater.* **2004**, *16*, 5495-5501.

(60) Lu, X.; Wang, R.; Yang, F.; Jiao, W.; Liu, W.; Hao, L.; He, X. Preparation of MoO3 QDs through combining intercalation and thermal exfoliation. *J. Mater. Chem. C* **2016**, *4*, 6720-6726.

(61) Nanayakkara, C. E.; Vega, A.; Liu, G.; Dezelah, C. L.; Kanjolia, R. K.; Chabal, Y. J. Role of Initial Precursor Chemisorption on Incubation Delay for Molybdenum Oxide Atomic Layer Deposition. *Chem. Mater.* **2016**, *28*, 8591-8597.

(62) Wang, G.; Ji, Y.; Zhang, L. H.; Zhu, Y. M.; Gouma, P. I.; Dudley, M. Synthesis of molybdenum oxide nanoplatelets during crystallization of the precursor gel from its hybrid nanocomposites. *Chem. Mater.* **2007**, *19*, 979-981.

(63) Shukoor, M. I.; Therese, H. A.; Gorgishvili, L.; Glasser, G.; Kolb, U.; Tremel, W. From layered molybdic acid to lower-dimensional nanostructures by intercalation of amines under ambient conditions. *Chem. Mater.* **2006**, *18*, 2144-2151.

(64) Hosono, K.; Matsubara, I.; Murayama, N.; Woosuck, S.; Izu, N. Synthesis of polypyrrole/MoO3 hybrid thin films and their volatile organic compound gas-sensing properties. *Chem. Mater.* **2005**, *17*, 349-354.

(65) Cong, S.; Sugahara, T.; Wei, T.; Jiu, J.; Hirose, Y.; Nagao, S.; Suganuma, K. Growth and Extension of One-Step Sol-Gel Derived Molybdenum Trioxide Nanorods via Controlling Citric Acid Decomposition Rate. *Cryst. Growth Des.* **2015**, *15*, 4536-4542.

(66) Badica, P. Preparation through the vapor transport and growth mechanism of the first-order hierarchical structures of

MoO3 belts on sillimanite fibers. *Cryst. Growth Des.* **2007**, *7*, 794-801.

(67) Akande, S. O.; Chroneos, A.; Vasilopoulou, M.; Kennou, S.; Schwingenschlögl, U. Vacancy formation in MoO3: hybrid density functional theory and photoemission experiments. *J. Mater. Chem. C* **2016**, *4*, 9526-9531.

(68) Scanlon, D. O.; Watson, G. W.; Payne, D. J.; Atkinson, G. R.; Egdell, R. G.; Law, D. S. L. Theoretical and Experimental Study of the Electronic Structures of MoO3 and MoO2. *The Journal of Physical Chemistry C* **2010**, *114*, 4636-4645.

(69) Li, X.-y.; Xiao, Q.-g.; Ning, P.-g.; Xu, H.-b.; Zhang, Y. Morphological and Structural Diversity of Molybdenum Oxide-Based Hybrid Materials Prepared through PEG Induction. *Cryst. Growth Des.* **2016**, *16*, 1512-1518.

(70) Irfan; Ding, H.; Gao, Y.; Small, C.; Kim, D. Y.; Subbiah, J.; So, F. Energy level evolution of air and oxygen exposed molybdenum trioxide films. *Appl. Phys. Lett.* **2010**, *96*, 243307.

(71) Chithambararaj, A.; Yogamalar, N. R.; Bose, A. C. Hydrothermally Synthesized h-MoO3 and alpha-MoO3 Nanocrystals: New Findings on Crystal-Structure-Dependent Charge Transport. *Cryst. Growth Des.* **2016**, *16*, 1984-1995.